Flow (2023), **1** E1
doi:XXXX

FLOW CAMBRIDGE UNIVERSITY PRESS

RESEARCH ARTICLE

Modification of Boundary Layer Turbulence by Submesoscale Flows

Leah Johnson*[1] and Baylor Fox-Kemper[2]

[1]Applied Physics Laboratory, University of Washington, Seattle, WA, 98105, USA
[2]Earth, Environmental, and Planetary Sciences, Brown University, Providence, RI, 02912, USA
*Corresponding author. E-mail: leahjohn@uw.edu

Received: XX 2023; **Revised:** XX XX 2023; **Accepted:** XX XX 2023

Keywords: Ocean Turbulence, Submesoscale, Boundary Layer, Potential Vorticity

Abstract

The mixing of heat and momentum in the ocean surface boundary layer (OSBL) is dominated by 1m to 10km fluid flows–too small to be resolved in global and regional ocean models. Instead, these processes are parameterized. Two main parameterizations include vertical mixing by surface forced meter-scale turbulence and overturning by kilometer-scale submesoscale frontal flows and instabilities. In present models, these distinct parameterizations are implemented in tandem, yet ignore meaningful interactions between these two scales that may influence net turbulent fluxes. Using a large eddy simulation of frontal spin down resolving processes at both scales, this work diagnoses submesoscale and surface forced turbulence impacts that are the foundation of OSBL parameterizations, following a traditional understanding of these flows. It will be shown that frontal circulations act to suppress the vertical buoyancy flux by surface forced turbulence and suggest OSBL parameterizations excessively mix buoyancy in the presence of lateral flows. These interactions have a direct influence on the upper ocean potential vorticity and energy budgets with implications for global upper ocean budgets and circulation.

Impact Statement

The ocean surface layer contains fluid flows that play an essential role in the communication between the atmosphere and ocean. Two small scale processes that are routinely approximated in global models include turbulent mixing due to atmospheric forcing and turbulent circulations from small scale currents. Interactions between surface-forced and current-forced turbulence indicate that our modeling approaches need updating.

1. Introduction

Turbulence in the ocean surface boundary layer (OSBL) involves a multitude of dynamics that drive fluid motions on a range of scales. This turbulence defines the boundary layer and therefore the upper ocean's role in transferring heat and momentum between the atmosphere and the ocean. Surface fluxes can drive fine-scale turbulence (O(1 cm) - O(100 m)) in the OSBL as energy injection from winds, waves, and cooling that compete with stratification by solar warming and freshwater fluxes (Belcher et al., 2012; Fox-Kemper et al., 2021). In the presence of strong lateral density variability, submesoscale fronts (O(50 m) - O(2 km): Bodner et al., 2023) and baroclinic mixed layer instabilities (O(500 m) - O(50 km): Dong et al., 2020) can restratify the upper ocean as dynamics release available potential energy to convert horizontal gradients into vertical ones (e.g., Fox-Kemper et al., 2008; Johnson et al., 2020). Additionally, a range of instabilities associated with O(1) Rossby number submesoscale

flows are known to drive energy in shear flows towards dissipative scales (Taylor and Ferrari (2009); Thomas et al. (2013)) producing turbulence comparable in length-scale (O(20 m) - O(500 m): Dong et al., 2021) but distinct from surface forced turbulence. The dynamic range of submesoscale and turbulent motions cannot be captured by global, regional, and even many submesoscale-permitting process models and therefore the unresolved motions are parameterized to a varying extent. The ability to parameterize transport by unresolved physics rests on averaging over the field of eddies, whether it be surface forced boundary layer turbulent eddies (e.g. Large et al., 1994; Umlauf and Burchard, 2003; Reichl and Hallberg, 2018; Troen and Mahrt, 1986), or larger, flatter eddies associated with baroclinic instabilities of mesoscale or submesoscale lateral density gradients (Gent and Mcwilliams, 1990; Fox-Kemper and Ferrari, 2008; Bodner and Fox-Kemper, 2020; Bachman et al., 2020). The theory of each parameterization targets a specific dynamical regime and isolates the time- and length-scales over which to average the processes to arrive at meaningful transport estimates. It is routine for global and regional circulation models to include separate parameterizations for boundary layer eddies and submesoscale eddies. Yet, implementing these individual processes in tandem typically ignores cross-scale interactions such as suppression of one scale of eddy by the eddies of the other scale. Note that this eddy-eddy effect is different from the effect a parameterization of one scale may have on the eddies of the other scale. For example, a parameterization of submesoscale restratification (Fox-Kemper et al., 2008) will reduce boundary layer depth and thus also reduce boundary layer eddy mixing because mixing strength scales with boundary layer depth (Monin and Obukhov, 1954). In the other direction, more surface forcing of a boundary layer parameterization will deepen the mixed layer and make submesoscale instabilities appear at larger scales. Here we focus on the eddy-eddy interaction in a multiscale simulation, not the parameterization-eddy interaction that could be carried out with a single scale resolved and the other parameterized. This work addresses how the foundational approximations for surface-forced boundary layer turbulence and submesoscale flows are modified when the two co-exist and interact in the OSBL.

Understanding nonlinear interactions between different eddying flows is a challenge due to the computational resources required for a large domain and small grid-scale simulations. A computationally approachable way to explore the role of boundary layer turbulence on submesoscale motions is through simulations that resolve submesoscale instabilities, yet parameterize boundary layer mixing (e.g. Mahadevan et al., 2010; Wyngaard, 2010; Callies and Ferrari, 2018; Wenegrat et al., 2020; Dauhajre and McWilliams, 2018), and has revealed how the evolution of submesoscale fronts is intimately linked to the turbulent environment they exist in. Yet these works are limited in their ability to understand how submesoscale flows impact fine-scale turbulence not resolved by such simulations. To do this, studies employ large eddy simulation (LES), with small enough grid scales (O(1m)) to resolve boundary layer eddies, yet large enough to simulate baroclinic waves and frontal instabilities (O(10km)). These simulations have been used to investigate the fine-scale motions associated with submesoscale flows (Verma et al., 2019; Skyllingstad and Samelson, 2012; Taylor and Ferrari, 2009), or how submesoscale fronts interact with wind-driven (Hamlington et al., 2014; Whitt et al., 2019; Skyllingstad et al., 2017) or convective (Thomas and Taylor, 2010; Verma et al., 2022; Skyllingstad et al., 2017) turbulence. Many of these studies identify the role of turbulence in enhancing or driving submesoscale circulation and the transfer of energy across spatial scales. Under a different lens, this work will revisit simulations presented in Hamlington et al. (2014) to understand how the interaction between fine-scale and submesoscale flows modify current idealized frameworks and state of the art parameterizations that treat them separately.

Section 2 overviews the LES and data used in the manuscript. Section 3 presents the multi-level Reynolds decomposition to separate different scales of motion. Section 4 reviews the buoyancy budget and evaluates how well different scales of transport relate to current scalings. These results are expanded to explore the impact of approximating turbulent flows using current state of the art turbulence parameterizations on the upper ocean PV budget in section 5, and to the impact on the dissipation rate of kinetic energy in section 6. Section 7 discusses these results in context of current work along with implications for steps forward.

2. Simulations and Data Summary

This work utilizes an LES of a frontal spin down under uniform wind stress and without waves (or Stokes drift) as described in Hamlington et al. (2014). Other studies have revisited passive tracers mimicking biological tracer transport (Smith et al., 2016), frontogenesis (Suzuki and Fox-Kemper, 2016), and potential vorticity spectra (Bodner and Fox-Kemper, 2020) in these runs; this analysis focuses on the standard diagnostic practices distinguishing turbulent "mixing" from submesoscale "overturning" underpinning parameterizations affecting buoyancy, energy, and potential vorticity.

The doubly periodic domain contains a warm filament with a uniform surface wind stress of $\tau = 0.025\,\mathrm{N\,m^{-2}}$ aligned at a 30^o angle from the geostrophic flow. It is convenient to divide the simulation spatially into three regions: 1) NOFRONT, 2) STABLE and 3) UNSTABLE (Fig. 1). The NOFRONT region represents the neutral BL, where turbulent motions are driven by surface wind stress and deliver modest entrainment. In the STABLE region, the constant and uniform, partly upfront, wind stress induces an Ekman transport to the right of the wind direction. This Ekman flow transports warm water over the cold side of the front (upfront wind/stable), thereby stratifying the boundary layer. In the UNSTABLE region, Ekman flow transports cold water over the warm side of the front, causing BL convection from the Ekman buoyancy flux (i.e., downfront winds; Thomas and Lee, 2005). This front develops unstable baroclinic instabilities that drive restratifying circulations within the boundary layer. The simulations were designed such that eddy restratification in this UNSTABLE region ($\mathrm{Q} \sim 25\,\mathrm{W\,m^{-2}}$) is larger than Ekman driven convection ($\mathrm{Q} \sim -13\,\mathrm{W\,m^{-2}}$) and similar in magnitude to the vertical heat flux in the NOFRONT region from shear driven mixing and entrainment ($\mathrm{Q} \sim -10\,\mathrm{W\,m^{-2}}$). Realistic forcing conditions might strengthen any one mechanism to dominate over the others (Haney et al., 2012). Note that the UNSTABLE region may also possess forced symmetric instabilities (Bachman et al., 2017). For the window of data analyzed, the STABLE and UNSTABLE regions are more stratified than the NOFRONT region, because of Ekman and mixed layer instability restratification, respectively. The fully developed eddy field and restratifying front at day 10 can be seen in Fig. 1.

Fluid motions in each of these domains are influenced by the dynamics on all scales, with velocity spectral slopes consistent with 2-D circulation involving frontal velocity jumps at larger scales (k^{-2} slope), transitioning to 3-D turbulence at $\sim 400\,\mathrm{m}$. Though velocity spectra support 3-D turbulence below 400 m, a detailed look at surface temperature (Fig. 1) reveals rich horizontal structure at the O(m) scale, thus challenging the assumption of horizontal homogeneity that often sets the prerequisite for OSBL turbulence physics (Monin and Obukhov, 1954). The goal is to evaluate how these finescale flows compare with buoyancy fluxes approximated by current OSBL parameterizations. To do this, three different OSBL parameterizations are implemented using the General Ocean Turbulence Modelling (GOTM; Burchard et al., 1999) framework (hereafter referred to as 1D) as summarized in Table 1:

Table 1. *List of parameterizations used in this study.*

abbr.	*description*	*citation*
GLS	General Length Scale	Umlauf and Burchard (2003)
CVMIX	K-Profile Parameterization	Van Roekel et al. (2018)
ePBL	Energetic Planetary BL	Reichl and Hallberg (2018)

The ingredients of extant submesoscale parameterizations (Fox-Kemper et al., 2008; Bachman et al., 2017) are diagnosed by scale separation.

3. Separation of Scales

Turbulent flows are often expressed in terms of their statistical mean through the Reynolds averaged equations, whereby instantaneous values are represented as the sum of an average value (in space or time)

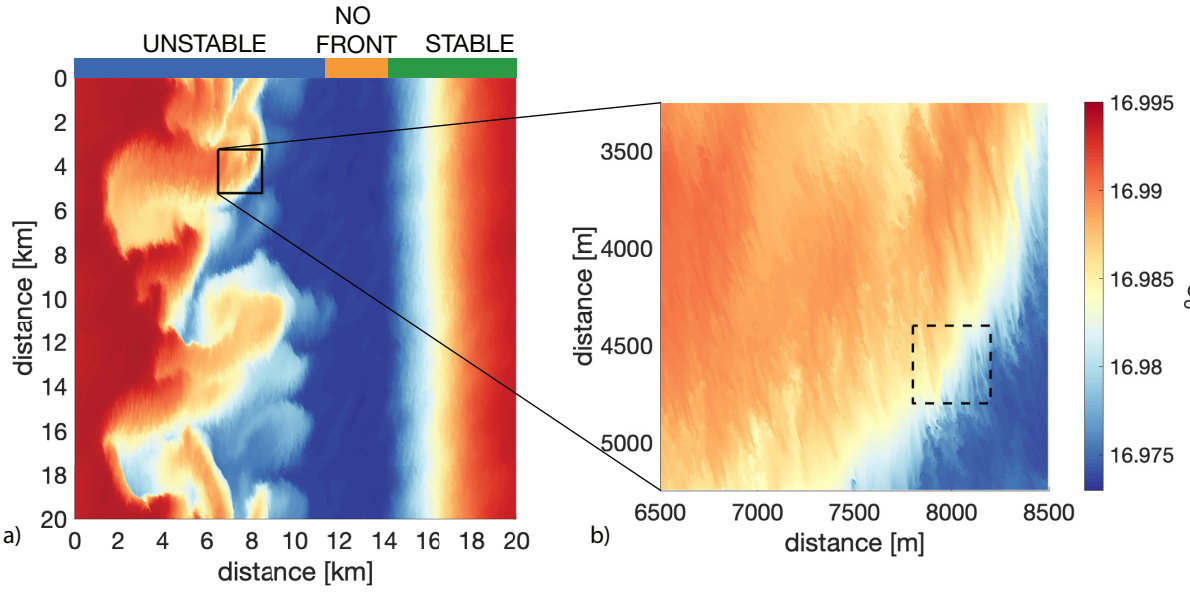

Figure 1. *Surface temperature at day 10 of the H14 runs. a) The entire model domain is separated into regimes: homogeneous turbulence region (NO FRONT - orange), front with stabilizing winds (STABLE - green), front with unstable winds and baroclinic instability (UNSTABLE - blue). b) a 2 km x 2 km close up of the UNSTABLE region. The dashed line is a 400 m x 400 m box, where 400 m length scale is the transition between quasi-2-D and 3-D flows (see H14). The colorbar is the same for both inserts.*

and fluctuations from the mean. The interpretation of the turbulence then, is subject to the resolution of the fluctuations and definition of the mean fields. Here, a multi-level Reynolds decomposition is utilized to separate submesoscale turbulence from finescale turbulence. The first decomposition for any variable c is $c = \tilde{c} + c'$, where $\tilde{c}$ represents a square boxcar average over a to-be-determined length scale to be permitted as submesoscale, and c' are the finer-than-submesoscale fluctuations from that mean. The submesoscale can also be averaged further along the front indicated by an overbar. Thus, $\tilde{c} = c^a + c^s$, where c^a is the along front average of $\tilde{c}$. The c^s are the submesoscale fluctuations from the along front mean. Combined, the decomposition becomes

$$c = \tilde{c} + c' = c^a + c^s + c', \;\; \tilde{c} = c^a + c^s, \;\; \overline{\tilde{c}} = c^a. \tag{1}$$

Note that c' is *not* the fluctuation term in a traditional along-front Reynolds decomposition, $c - \overline{c} \neq c'$, it is the fluctuation from a submesoscale-permitting resolution as in (1)–similar to the role that a boundary-layer mixing parameterization would play in a submesoscale-permitting model (e.g., Gula et al., 2014; Su et al., 2018). On the other hand, the submesoscale-permitting mean, $\tilde{c}$, may be analogous to a coarse resolution regional or process model that resolves submesoscale turbulence but not finescale motions, which is parameterized. Making this scale-separation specific then rests on the definition of the minimum submesoscale length permitted in $\tilde{c}$. A sensible definition is the transition scale from 2-D to 3-D turbulence scaling. Our choice is 399.5 m, based on the 400 m flow transition for this simulation described in Hamlington et al. (2014) and Bodner and Fox-Kemper (2020).

The along-front and submesoscale mean are both linear operators, and they are furthermore idempotent Reynolds averages, which distinguishes them from more generic "linear filters" more commonly used in LES (e.g., Fox-Kemper and Menemenlis, 2008; Storer et al., 2022). Differentiation and integration are also linear operators, but they do not commute with averaging generally. A further discussion

of the specific operators used, their limitations and estimates of error resulting from these choices is in the appendix.

The multi-level Reynolds decomposition for a Boussinesq fluid is thus

$$\frac{\partial}{\partial t}\left(b^a + b^s + b'\right) = -\frac{\partial}{\partial x_j}\left[\left(u_j^a + u_j^s + u_j'\right)\left(b^a + b^s + b'\right)\right] - \mathcal{V}_{ij}^b \tag{2}$$

$$\begin{aligned}\frac{\partial}{\partial t}\left(u_i^a + u_i^s + u_i'\right) = &-\frac{\partial}{\partial x_j}\left[\left(u_j^a + u_j^s + u_j'\right)\left(u_i^a + u_i^s + u_i'\right)\right] - \frac{1}{\rho_o}\frac{\partial}{\partial x_i}\left(p^a + p^s + p'\right) \\ &- 2\epsilon_{ikj}\Omega_j\left(u_k^a + u_k^s + u_k'\right) - \mathcal{V}_{ij}^m.\end{aligned} \tag{3}$$

Here, b is buoyancy, u is velocity, p is pressure, Ω is planetary rotation rate and $\mathcal{V}_{ij}^b$ and $\mathcal{V}_{ij}^m$ are the divergence of the diffusive buoyancy and viscous momentum fluxes respectively. Taking first the submesoscale Reynolds average (noting that all terms linear in primes vanish) and then the along-front average (noting that all terms linear in submesoscale variables vanish) of Eq. (2) and Eq. (3), yields the multi-level Reynolds averaged equations for along front mean of buoyancy and momentum:

$$\frac{\partial b^a}{\partial t} = -\frac{\partial}{\partial x_j}\left[u_j^a b^a\right] - \frac{\partial}{\partial x_j}\widetilde{\overline{b^s u_j^s}} - \frac{\partial}{\partial x_j}\widetilde{\overline{b' u_j'}} - \widetilde{\overline{\mathcal{V}_{ij}^b}} \tag{4}$$

and

$$\frac{\partial u_i^a}{\partial t} = -\frac{\partial}{\partial x_j}\left[u_j^a u_i^a\right] - \frac{1}{\rho_o}\frac{\partial p^a}{\partial x_i} - 2\epsilon_{ikj}\Omega_j u_k^a + \frac{\partial}{\partial x_j}\widetilde{\overline{u_i^s u_j^s}} - \frac{\partial}{\partial x_j}\widetilde{\overline{u_i' u_j'}} - \widetilde{\overline{\mathcal{V}_{ij}^m}}, \tag{5}$$

The covariance terms capture transport of properties at the different scales, separating clearly the transport by submesoscale turbulence from transport due to fine-scale motions.

This Reynolds-averaging approach is more similar to the scale-separation assumption typical of ocean climate models (i.e., scale-separated Reynolds averaging) rather than cascade-filtering approaches more typical to large eddy simulation studies (see, e.g., Fox-Kemper and Menemenlis, 2008; Aluie et al., 2018). The reason for the choice of Reynolds averaging is to explore whether the approach taken in ocean climate modeling is deficient when considering both the turbulence of the submesoscale (e.g., Fox-Kemper et al., 2008) and the fine-scale (e.g., Large et al., 1994), potentially including resolving the submesoscale but not the fine-scale (e.g., Gula et al., 2014; Su et al., 2018). Note that these scales are neighboring, but spectrally distinct in this simulation and recognizable as quasi-2-D and 3-D cascades (Hamlington et al., 2014; Bodner and Fox-Kemper, 2020). Eq. (4) is similar to the triple decomposition used with observations to evaluate along isopycnal tracer dispersion in the North Atlantic (Ferrari and Polzin, 2005; Smith and Ferrari, 2009) and Southern Ocean (Garabato et al., 2016) stratified ocean interior, but here the decomposition is used in the context of the OSBL. This Reynolds decomposition will be used to evaluate the role of multi-scale transport on the upper ocean buoyancy budget in a form that lends itself to being compared with current subgridscale parameterizations.

Submesoscale motions manifest in the buoyancy and energy budgets and are linked to the fluid's potential vorticity. In terms of the buoyancy budget and energetics, (Fox-Kemper et al., 2008, 2011), submesoscales impact stratification and enhance the transfer of energy towards dissipative scales (Capet et al., 2008; Thomas and Taylor, 2010; Taylor and Ferrari, 2010; McWilliams, 2016). Additionally, potential vorticity is a dynamically relevant tracer to understand and identify submesoscale processes (Johnson et al., 2020; Bodner and Fox-Kemper, 2020), especially symmetric instability (Hoskins, 1974; Thomas et al., 2013; Haney et al., 2015; Bachman et al., 2017). The following sections evaluate the roles of submesoscales and turbulent scales on the tendencies of upper ocean buoyancy and potential vorticity as well as on the dissipation of kinetic energy.

4. The Buoyancy Budget

4.1. The Transformed Eulerian Mean with mixing

When averaged in the along front direction and neglecting viscous dissipation, the Reynolds averaged equation for buoyancy, Eq. (6), can be re-written as

$$\frac{\partial b^a}{\partial t} = -\bar{v}M^2 - \bar{w}N^2 - \frac{\partial}{\partial y}\overline{b^s v^s} - \frac{\partial}{\partial z}\overline{w^s b^s} - \frac{\partial}{\partial y}\overline{v'b'} - \frac{\partial}{\partial z}\overline{w'b'} \tag{6}$$

where $M^2 = \partial b^a/\partial y$ and $N^2 = \partial b^a/\partial z$ are horizontal and vertical gradients of the along front averaged buoyancy, respectively. The mean circulation (first two terms of Eq. (6)) is driven mostly by the injection of horizontal vorticity by the winds, resulting in an Ekman transport to the right of the windstress. This Ekman overturning is represented by the Eulerian mean streamfunction, Ψ^a, where $v^a = \partial\Psi^a/\partial z$ and $w^a = -\partial\Psi^a/\partial y$. In the stable region, Ekman overturning restratifies the front, as differential advection moves warmer water (less dense) over the cold (more dense) side of the front. In the UNSTABLE region, Ekman transport advects dense (cold) water over light (warm), resulting in convection. This destabilizing Ekman overturning is opposed by eddy driven overturning that acts to restratify the front (terms 3 and 4 in Eq. (6)). The eddy overturning is diagnosed by the Held and Schneider (1999) streamfunction:

$$\Psi^s = -\frac{\overline{w^s b^s}}{M^2}. \tag{7}$$

Recognizing the eddy-induced transport slope (S) and the isopycnal slope (I) as:

$$S \equiv \frac{\overline{w^s b^s}}{\overline{v^s b^s}}, \qquad I \equiv \frac{-M^2}{N^2}, \tag{8}$$

an eddy forcing term (Held and Schneider, 1999) can then be defined as:

$$T_* \equiv \overline{v^s b^s}\left(1 - \frac{S}{I}\right). \tag{9}$$

If more tracers were present (per Smith et al., 2016) and used in the analysis of the submesoscale transport, a method like the one used in Bachman et al. (2015, 2020) might reveal that the eddy-induced transport has more structure than just a streamfunction.

Finally, under the assumption that finescale mixing is dominated by 3-D turbulence that is anisotropic according to the surface orientation, the last terms on the RHS of Eq. (4) can be written using k-theory as an eddy diffusivity, such that $\overline{w'b'} = -\kappa_v N^2$ and $\overline{v'b'} = -\kappa_h M^2$.

The buoyancy budget can now be written as:

$$\frac{\partial b}{\partial t} = \underbrace{\nabla\cdot(\Psi^a \times \nabla b^a)}_{\text{Ekman}} + \underbrace{\nabla\cdot(\Psi^s \times \nabla b^a)}_{\text{Eddies}} + \underbrace{\frac{\partial}{\partial z}\left(\kappa_v N^2\right)}_{\text{Turbulence}} + \underbrace{\frac{\partial}{\partial y}\left(T_* + \kappa_h M^2\right)}_{\text{Residual}}. \tag{10}$$

We note that the form of these diagnosed quantities is not guaranteed to be the most meaningful but is chosen to match the parameterization forms presently in use.

Combining *Ekman* and *Eddy* streamfunctions, $\Psi^{tem} = \Psi^a + \Psi^s$, (e.g Held and Schneider, 1999; Marshall and Radko, 2003), transforms Eq. (10) into the classic Transform Eulerian Mean (TEM) equations modified to include finescale mixing. The inclusion of the Turbulence term is particularly important in the near surface ocean where strong surface forcing can cause finescale advective fluxes that compete with submesoscale and mean transports. This work will focus on the contribution of the first three terms, Ekman, Eddies and Turbulence, to stratification. Overall, along-front frontogenesis is

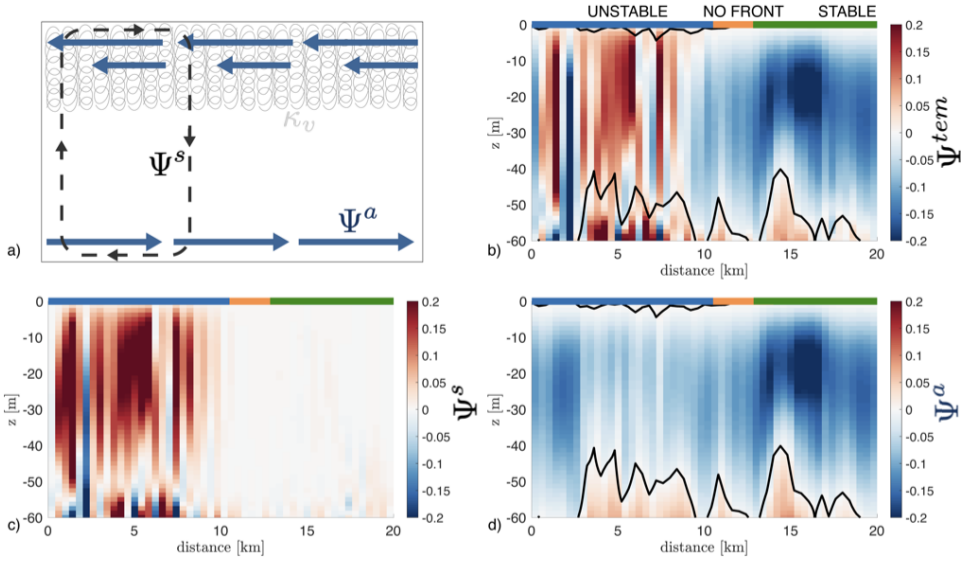

Figure 2. *Overturning streamfunctions. a) Schematic representing the different components of the buoyancy budget. Blue arrows - Ekman overturning. Grey dashed line - submesoscale eddy overturning. Light grey curls - wind driven mixing. b) The sum of the Ekman streamfunction (Ψ^a calculated from along front velocities) and the Held and Schnieder streamfunction (Ψ^s in Eq. (4.1)). Note that the positive circulation in the UNSTABLE region is consistent with dominating eddy restratification c) Held and Schnieder streamfunction (Ψ^s), only. d) Ekman overturning (Ψ^a), only*

not expected to be strong in this configuration due to a lack of large-scale strain, but it is included in the Ekman term if present. Submesoscale frontogenesis (Suzuki and Fox-Kemper, 2016) involves fronts that deviate from the along-channel direction and thus are likely to be strongest in the Eddies term.

4.2. Scaling buoyancy fluxes

Focusing on stratification, it is common to compare the relative strength of the vertical buoyancy flux associated with the first three terms on the RHS of Eq. (10). These scalings are:

$$\underbrace{w^a b^a \sim \frac{\tau \times \hat{k}}{\rho} M^2}_{\text{Ekman Buoyancy Flux}} \qquad \underbrace{\overline{w^s b^s} \sim C_e \frac{M^4 H^2}{f}}_{\text{Mixed Layer Eddies}} \qquad \underbrace{\overline{w' b'} \sim -\kappa N^2}_{\text{k-theory Turbulence}} . \tag{11}$$

The first term (Ekman Buoyancy Flux, or EBF: Thomas and Lee, 2005) represents differential advection of horizontal buoyancy gradients by Ekman transport, (Fig. 2 a, d), causing a destablizing buoyancy flux in the UNSTABLE region and a restratifying buoyancy flux in the STABLE region. The second term is specific to the UNSTABLE region, where baroclinic instability drives a restratifying submesoscale eddy overturning (Mixed Layer Eddies, or MLE: Fox-Kemper et al., 2008), as in Fig. 2a,b,c. Previous work has evaluated the tradeoff between destratifying Ekman transport and restratifying submesoscale eddies using the EBF and MLE scalings (e.g. Taylor and Ferrari, 2011; Mahadevan et al., 2010). Finally, the last term is relevant to all regions, as wind stress injects energy into finescale motions, approximated in k-theory as an isotropic, downgradient eddy diffusivity, κ (e.g. Large et al., 1994; Reichl and Hallberg, 2018; Umlauf and Burchard, 2003).

Values for Ψ and an effective mixing coefficient, κ_{eff}, can be calculated from the numerical simulation directly using Eq. (11) and compared with current scalings and parameterizations that also estimate the

vertical structure of these effects (see Fig. 3). Scalings are estimated using the mean fields on days 10 and 11 (i.e. well developed circulations), not the initial field, which had ~ 5 times stronger horizontal buoyancy gradient initially. The focus here is to assess how well parameterizations for κ, derived from theory in a homogenous boundary layer, represent finescale vertical mixing of buoyancy, $\overline{w'b'}$. Yet it is useful to also evaluate how the other scalings agree with the mean wind driven and submesoscale overturning.

As anticipated, the submesoscale vertical buoyancy flux is active in the presence of baroclinic waves (UNSTABLE) and negligible in the other regions (Fig. 3a,d; Fig. 2c). In the UNSTABLE region, MLE restratification scales as expected, with a vertical profile of $\overline{w^s b^s}$ similar to that predicted (Ψ_{MLE}) by Fox-Kemper et al. (2008) and a vertically averaged $\overline{w^s b^s}$ ($4.4 \times 10^{-10} m^2 s^{-3}$) within 6% of the Ψ_{MLE} prediction.

The interpretation of mean $\overline{w^a b^a}$ through EBF is more nuanced. The weakening of the fronts during spin down implies that EBF scales are stronger than MLE for the data analyzed. This stronger EBF is not found in $\overline{w^a b^a}$ (Fig. 3d). In UNSTABLE, $\overline{w^a b^a}$ ($4.4 \times 10^{-10}\,\mathrm{m^2\,s^{-3}}$) is similar and opposite to MLE, while in STABLE $\overline{w^a b^a}$ is smaller yet ($2.4 \times 10^{-10}\,\mathrm{m^2\,s^{-3}}$), balancing $\overline{w^t b^t}$. The scaling for EBF is rooted in horizontal advection of buoyancy by Ekman transport and so can also be compared with vertically averaged over the Ekman depth, which yields ($6.5 \times 10^{-10}\,\mathrm{m^2\,s^{-3}}$) in UNSTABLE and $1.6 \times 10^{-9}\,\mathrm{m^2\,s^{-3}}$ in STABLE. Some of the differences may be the result of geostrophic stress excluded from the classical EBF scaling (Wenegrat and McPhaden, 2016). Overall, the asymmetry in horizontal and vertical transport highlights nonlinear interactions that complicate the interpretation of EBF in well developed flows. Ultimately, the interplay between horizontal vorticity injection by winds and restratification by the resulting overturning alters the Ekman overturning streamfunction.

Though surface forcing is uniform throughout, finescale turbulent fluxes $\overline{w'b'}$ vary across regimes as mean Ekman overturning and submesoscale flows interact with transport by wind driven BL eddies (Fig. 3b). This multi-scale interaction has implications for effective κ_{eff} in each region (Fig. 3c). The smallest $\overline{w'b'}$ magnitude is in NOFRONT, absent of lateral buoyancy advection. Using the Monin and Obukhov (1954) similarity theory to arrive at non-dimensional κ_{eff} in NOFRONT scales reasonably well with traditional 1D BL turbulence parameterizations, being within 20% of ePBL and GLS, but with KPP exceeding diagnosed mixing by 60%.

The agreement between 1D and κ_{eff} falls off in the frontal regions. In STABLE, turbulent fluxes are negative and larger in magnitude than the no front region as turbulent eddies drive down warm water advected near the surface by Ekman shear. The larger magnitude $\overline{w'b'}$ than NOFRONT is expected as enhanced stratification implies there is more buoyancy to flux. Yet the Monin and Obukhov (1954) non-dimensional mixing κ_{eff} in this region is smaller than NOFRONT and 1D, so turbulence is suppressed in the retratifying STABLE region compared to BL scalings. This may seem obvious as lateral restratification is expected to suppress turbulence, but this suppression is *stronger* than Monin and Obukhov (1954) scaling predicts. These results are not trivial, particularly for similarity based parameterizations where surface fluxes are intrinsic to the mixing amplitude and do not include information about lateral fluxes and lateral gradients–note that Monin and Obukhov (1954) assumes horizontal homogeneity with prohibits both. This implies that suppressed turbulence by lateral restratification is not well represented in 1D, and that current turbulence parameterizations are systematically over-mixing surface layers in the presence of lateral gradients and flows.

Turbulent buoyancy flux with NOFRONT and STABLE are both negative (positive κ_{eff}), consistent with the classic k-theory assumption that turbulence can be approximated as an eddy diffusivity mixing a flux down gradient. This assumption breaks down in the UNSTABLE region, as $\overline{w'b'}$ becomes positive in the presence of positive mean N^2. The positive $\overline{w'b'}$ is not uniform across the region, but $\overline{w'b'}$ varies spatially ranging from -2×10^{-10} to 1×10^{-9}. Isolating regions of the strongest buoyancy gradients ($|\nabla_H b|$ stronger than the initial front $M_0^2 = 2.1 \times 10^{-8}\,\mathrm{s^{-2}}$) and regions of negative PV confirm that finescale circulations within the sharpest portions of the front are transporting buoyancy upward and against mean stratification, thereby resulting in negative κ_{eff}. A negative diagnosed κ_{eff} may be associated

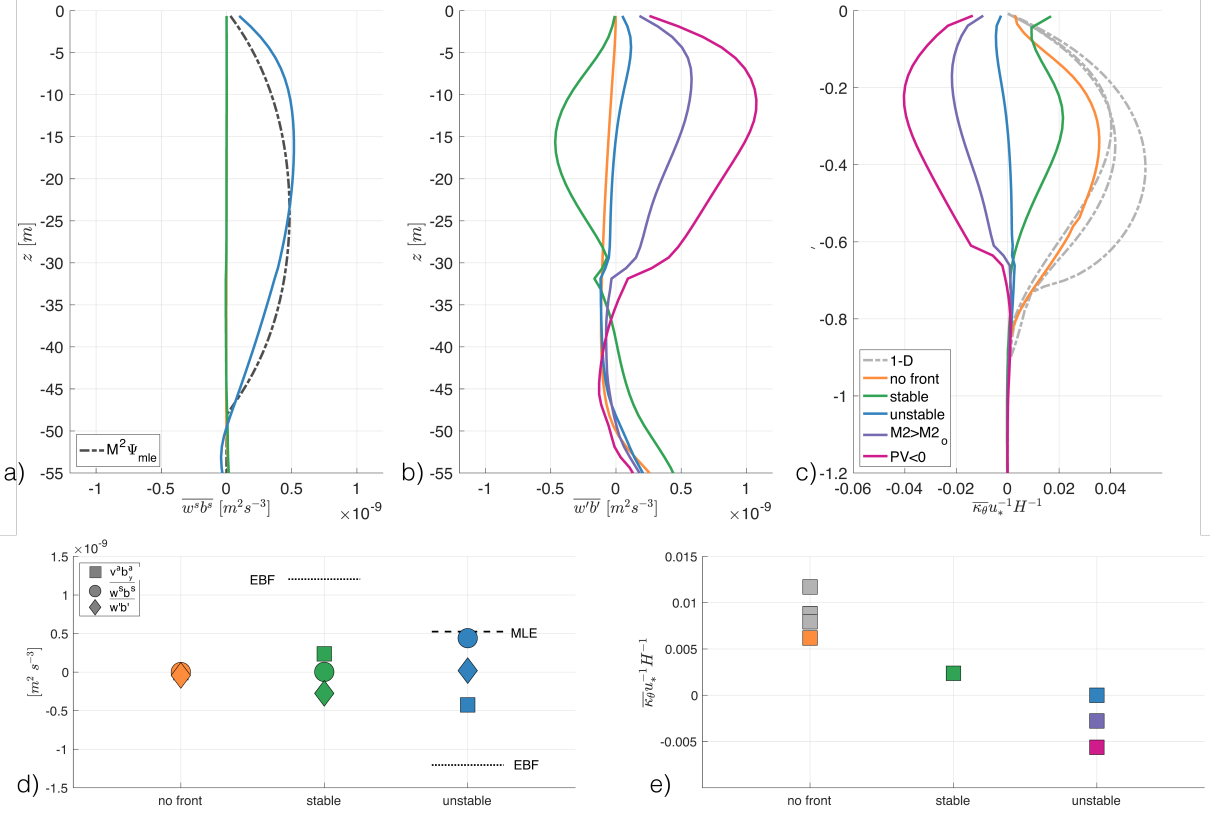

Figure 3. *Buoyancy fluxes for different regions across the front, and colors across subplots follow the legend in (c). a) Submesoscale buoyancy flux, $\overline{w^s b^s}$ as in Eq. (4.1) . The only notable flux is in the UNSTABLE region and agrees with Ψ_{MLE} of Fox-Kemper et al. (2008). b) turbulent buoyancy flux across regions. Negative $\overline{w'b'}$ for the NOFRONT and STABLE regions is consistent with down-gradient mixing and positive diffusivity in c). The UNSTABLE region has a net positive $\overline{w'b'}$ at depths less than 15 m in the presence of stable stratification, consistent with a counter gradient flux or frontal overturning. Averaging only in regions where lateral stratification is particularly strong and UNSTABLE (purple) or where potential vorticity is negative (magenta) increases the degree of counter-gradient flux. c) Turbulent diffusivity, κ_{eff}, is estimated as $\overline{w'b'}/N^2$ and is compared against κ produced by three OSBL parameterizations, k-eps, ePBL and KPP. Note that in UNSTABLE, strong M^2, and negative PV regions these parameterizations produce the wrong sign of diffusivity and in the STABLE region they overestimate the diffusivity. d) ML averaged buoyancy fluxes for mean, submesoscale and turbulent fields across domains. Dashed lines mark the classic scalings (Eq. 11) for EBF and MLE. e) ML averaged κ_{eff} across domains, normalized by H and u_**

with (non-local) convective instabilities or a result of frontal restratifying overturning circulations (as in the lateral-instability-driven circulations of Sullivan and McWilliams, 2019) which might be represented by the HS streamfunction, but here this effect is occurring on scales *finer than the submesoscale*. Therefore, the near zero $\overline{w'b'}$ in the UNSTABLE region does not imply that finescale fluxes are not important, rather finescale fluxes are transporting significant buoyancy upgradient to counter balance the mixing downgradient by surface forced boundary layer eddies. This finescale circulation is not captured by coarser grain models that implement submesoscale parameterizations alongside OSBL

parameterizations, and again suggests these models are over-mixing buoyancy in the presence of lateral gradients and flows.

5. PV Fluxes

The full Ertel PV, q, is defined as

$$q = (f\delta_{i3} + \omega_i)\,\frac{\partial b}{\partial x_i} \tag{12}$$

where $\omega_i = \varepsilon_{ijk}\frac{\partial u_k}{\partial x_j}$ and subscript index 3 is taken to be the rotation axis direction (vertical).

The nonlinearity that arises from the correlation between velocity gradients and buoyancy gradients implies that $\overline{(f\delta_{i3} + \omega_i')\partial b'/\partial x_i} \neq 0$, and that small scale gradients impact mean PV. In a turbulent regime, PV at the small scale has a different behavior than those expected from geophysical fluids (Bodner and Fox-Kemper, 2020) as small scale correlations create noisy fluctuations that dominate mean PV even on larger scales. Bodner and Fox-Kemper (2020) suggest that pre-filtered buoyancy and momentum be used to define PV in Large Eddy Simulations and that turbulent scale momentum and buoyancy fluxes be contained as a turbulent flux divergence. Therefore, PV relevant to geophysical flows is defined by submesoscale or larger fields, but the tendency of PV may be altered by finescale processes. The following section adopts the approach of Bodner and Fox-Kemper (2020) for the Reynolds averaged equations, thus adapting it to be comparable with BL parameterizations.

When defining the submesoscale potential vorticity ($\tilde{q}$), the Reynolds average includes the submesoscale-permitting fields only, $\tilde{c}$, not yet averaged in the along front direction. A full derivation of the PV in the multi-Reynolds decomposition, the Mean-Eddy PV (MEPV) can be found in Appendix B. The submesoscale-permitting PV is

$$\tilde{q} = (f\delta_{k3} + \tilde{\omega}_i)\,\frac{\partial \tilde{b}}{\partial x_i}, \tag{13}$$

In the full MEPV decomposition (Appendix B), the $\overline{\omega_i^s \partial b^s/\partial x_i}$ contributes $1-5\%$ of $\tilde{q}$, yet it will be shown that submesoscale fluctuations play a leading order role in $\tilde{q}$ tendencies.

Following Bodner and Fox-Kemper (2020), derivation of the subPV tendency equation begins with the combining the turbulent transport terms into frictional and diffusive fluxes by defining:

$$\mathcal{F}_i^+ = -\frac{\partial}{\partial x_j}\left(\widetilde{u_i'u_j'}\right) - \mathcal{V}_{ij}^m; \tag{14}$$

$$\mathcal{D}^+ = -\frac{\partial}{\partial x_j}\left(\widetilde{b'u_j'}\right) - \mathcal{V}_{ij}^b; \tag{15}$$

Note that Eq. (14) and Eq. (15) assume that Reynolds-averaging to the submesoscale-permitting scale ($\tilde{\cdot}$) commutes with differentiation. The uncertainty in (14) and (15) implied by the finescale variations in the choice of boundary locations for the $\tilde{\cdot}$ average can be estimated from Leibniz's theorem and gives an error estimate for the horizontal derivatives that are an order of magnitude larger than the signal (see Appendix A). Nonetheless, the Reynolds averaged expression is most analogous to the parameterized form for turbulence solved by submesoscale-permitting simulations. Evaluating PV in this framework, in light of these uncertainties, allows a comparison between how PV is modeled in larger grid-scale ocean simulations to the $\tilde{q}$ in the LES.

The $\tilde{q}$ tendency equation can be found by multiplying the $\tilde{u}$ evolution equation by $\partial\widetilde{b}/\partial x^i$, and multiplying the $\tilde{b}$ evolution equation by $(f\delta_{k3} + \widetilde{\omega}_i)$ (Appendix B). Combining the two and rearranging

gives the PV evolution in flux form:

$$\frac{\partial}{\partial t}\tilde{q} = -\frac{\partial}{\partial x_i}\left[\underbrace{\widetilde{u}_i\widetilde{q}}_{\text{ADV}} + \underbrace{\epsilon_{ikj}F_j^+\frac{\partial\widetilde{b}}{\partial x_k}}_{\text{FRIC}} - \underbrace{(f\delta_{k3}+\widetilde{\omega})\,\mathcal{D}^+}_{\text{DIA}}\right] \tag{16}$$

The advective flux (ADV) includes correlations between submesoscale currents and submesoscale gradients that define $\tilde{q}$. Similarly, turbulent scale motions interact with submesoscale buoyancy gradients through the friction (FRIC) and diabatic (DIA) flux terms.

The divergences of the ADV, FRIC, and DIA terms are estimated from the upper 30 m in the LES regions, to avoid noise near the ML base. The magnitude of these terms for each region is shown in Fig. 4.

In the STABLE region, ADV increases PV, consistent with Ekman overturning which drives restratification while DIA competes with ADV to decrease PV. The process underlying DIA's reduction of PV is dominated by submesoscale correlations between the vertical buoyancy flux divergence and vertical vorticity as wind driven turbulent motions homogenize buoyancy in the presence of geostrophic frontal flow.

In the UNSTABLE region, ADV, FRIC and DIA all increase PV, consistent with the dominance of MLE restratification over destratifying Ekman overturning in the buoyancy budget discussed in section 4. Small scale diabatic mixing (DIA) increases PV as positive vertical buoyancy flux interacts with vertical vorticity gradients near sharp fronts. The tendency for finescale turbulence to increase PV is reminiscent of the injection of PV into the mixed layer (ADV) by baroclinic instability as described by (Boccaletti et al., 2007) as well as due to frictional geostrophic stress (FRIC) at the surface (Wenegrat and McPhaden, 2016) and secondary instabilities such as symmetric instability (Thomas et al., 2013).

In section 4, the diffusivities (κ_{eff}) in the unstable and stable regions are markedly different from that predicted by current state of the art OSBL parameterizations. It is therefore of interest to explore how approximating turbulent fluxes with an OSBL parameterization might impact PV tendency (Fig. 4 light shading for parameterizations). Parameterized turbulence from GOTM can easily be used to replace the turbulent flux divergences in Eqs. (14) and (15) with the following (assuming isotropic mixing on finescales):

$$\mathcal{F}_j^+ \rightarrow \mathcal{F}^{\text{param}} = \frac{\partial}{\partial x_j}\left(\nu_H\frac{\partial\widetilde{u}_i^a}{\partial x_j}\right) \tag{17}$$

$$\mathcal{D}^+ \rightarrow \mathcal{D}^{\text{param}} = \frac{\partial}{\partial x_j}\left(\kappa_H\frac{\partial\widetilde{b}^a}{\partial x_j}\right) \tag{18}$$

where ν_H and κ_H are from the GOTM 1D models' ML eddy viscosity and diffusivity respectively. The mixing coefficients ν_H and κ_H are specific to each submesoscale average grid and estimated using the average of the non-dimensionalized 1D κ, i.e., take the average of $\kappa_\theta {u_*}^{-1} H^{-1}$ over the ensemble of 1D models in Fig. 3. The dimensional diffusivity and viscosity are then restored (per Monin and Obukhov, 1954), by multiplying the average by the local u_*H for each submesoscale bin. This PARAM estimate is analogous to what would occur in a submesoscale-permitting model that uses parameterized turbulence in the form $\kappa_c = \mu v_t l$, where μ is a non-dimensional coefficient, v_t is the turbulent velocity scale (proportional to u_*) and l is a typical turbulence length scale proportional to the depth of the boundary layer (i.e., H) (Tennekes and Lumley, 2018; Large et al., 1994)). Further assumptions are isotropy and that the Prandtl number is assumed equal to one, $Pr = \nu_H/\kappa_H = 1$, so $\nu_V = \nu_H = \kappa_V = \kappa_H$. With these assumptions and Eqs. (14)-(15) and (17)-(18), the PV fluxes of the parameterizations are found. The vertical gradients dominate the flux divergence, accounting for 99% of the fluxes.

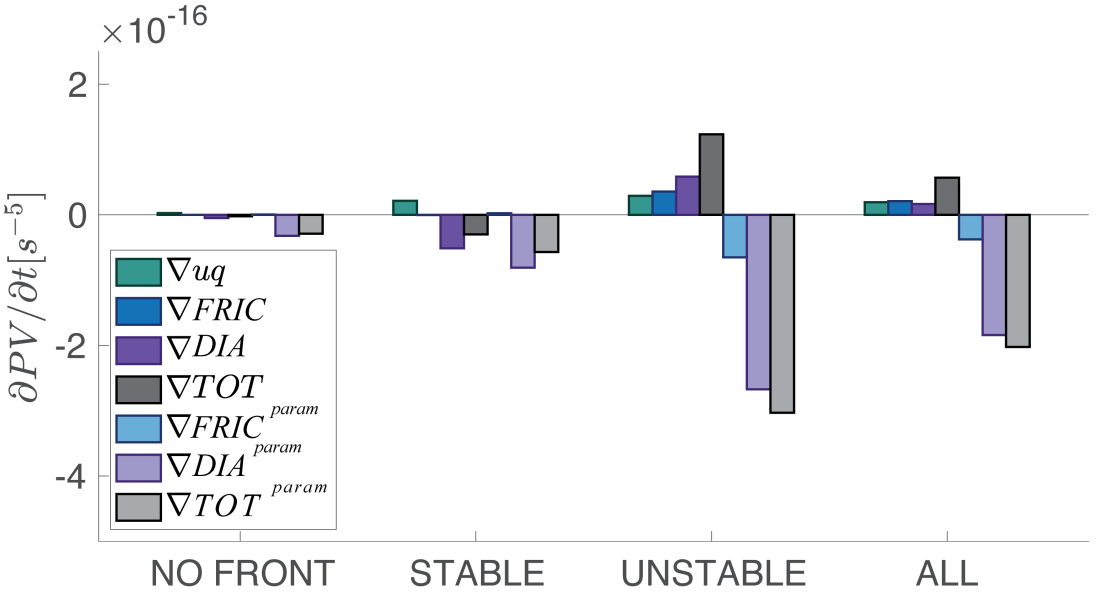

Figure 4. *MEPV tendency equation terms separated by region as described in Eq. (16). Green is $\partial/\partial x_i(ADV)$, blue is $\partial/\partial x_i(FRIC)$, purple is $\partial/\partial x_i(DIA)$ and dark grey is the sum of all three terms. Light blue and light purple represent the parameterized equivalent of $FRIC$ and DIA, where the LES turbulent fluxes have been replaced with parameterized fluxes estimated from 1D models (see Table 2). Light grey is the sum of the advective term (green) and the parameterized terms (light blue and light purple).*

In the STABLE region, $\mathcal{F}^{\text{param}}$ and $\mathcal{D}^{\text{param}}$ are of opposite sign, but $\mathcal{D}^{\text{param}}$ and their sum are much larger in magnitude than $\mathcal{F}^{+}$ and $\mathcal{D}^{+}$ (Fig. 4). The dominant signal is the overestimation of $\mathcal{D}^{\text{param}}$, consistent with the results in 4, where the resolved turbulent flux of buoyancy in the STABLE region was suppressed compared to parameterized fluxes and Monin-Obukhov scaling. However, in the dimensionless diffusivities, this suppression was only a factor of two (Fig. 3c), whereas $\mathcal{D}^{\text{param}}$ is more than four times $\mathcal{D}^{+}$ indicating that the averaged gradients and covariation over a submesoscale gridscale lead to further errors.

In the UNSTABLE region, $\mathcal{F}^{\text{param}}$ and $\mathcal{D}^{\text{param}}$ are of the same sign, but both are larger in magnitude and *of opposite sign* to their turbulence diagnosis partners $\mathcal{F}^{+}$ and $\mathcal{D}^{+}$ (Fig. 4). Again, $\mathcal{D}^{\text{param}}$ dominates the parameterized PV tendency terms, as parameterized fluxes mix buoyancy down gradient. The positive $\mathcal{D}^{+}$ from finescale PV injection into the ML is not captured by the parameterized mixing $\mathcal{D}^{\text{param}}$, thereby inaccurately representing PV changes in the presence of unstable flows. Therefore, in both STABLE and UNSTABLE, but for different reasons, parameterized mixing tends to drive PV toward negative values–in the opposite direction or faster than implied by the resolved LES finescale turbulent fluxes. Over the whole domain, this implies that the parameterizations predict a completely inaccurate PV budget, which should be a caution for using even the sign of PV fluxes as inferred from parameterizations.

6. Dissipation of Kinetic Energy

Instabilities of submesoscale frontal flows are known to transfer energy to smaller scales, thereby enhancing the dissipation of kinetic energy. Terms in the turbulent or eddy kinetic energy equations, often used to gain insight into transfer pathways for energy towards smaller scales, are difficult to estimate locally (Cao et al., 2021) and therefore are not calculated here. Yet the dissipation rate of kinetic energy,

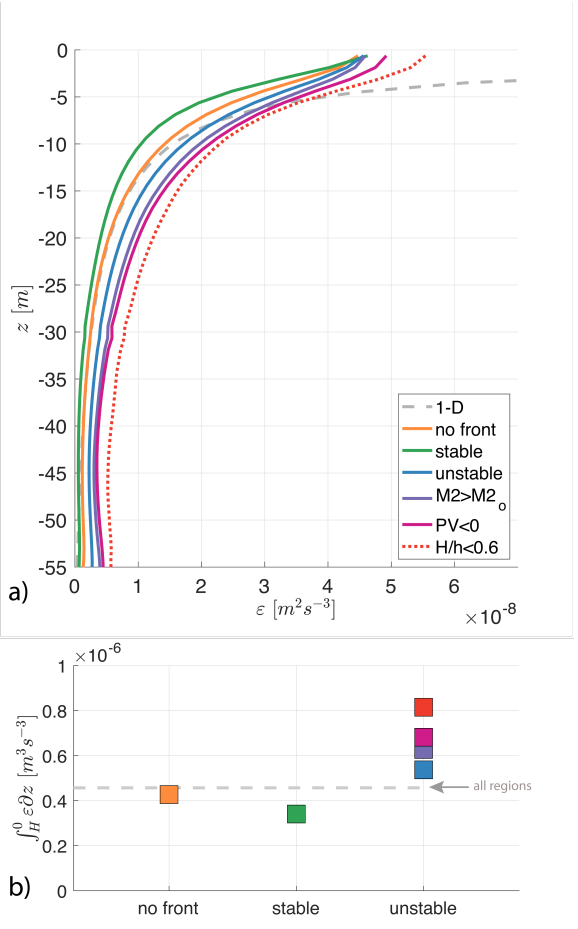

Figure 5. *a) Profiles of turbulent energy dissipation averaged over different regions of the domain, $\overline{\epsilon}$ including NOFRNT (orange), STABLE (green) UNSTABLE (blue), UNSTABLE region with $M^2 > M_o^2$ (purple), UNSTABLE region with PV < 0 (magenta), and UNSTABLE region with $H/h < 0.6$ (red dashed). GLS ϵ is included for reference (grey dashed line). b) Depth- and region averages of $\overline{\epsilon}$ with colors corresponding to lines in (a). The grey dashed line in the average ϵ across the domain.*

ϵ can be averaged over domains and is used here to understand how energy is dissipated in the presence of submesoscale fronts. Following Sullivan et al. (1994) and Bodner and Fox-Kemper (2020), the grid scale dissipation rate, ϵ, is calculated from the subgrid turbulent kinetic energy. Profiles of $\overline{\epsilon}$ (Fig. 5a) from each region are compared with that estimated from GLS (Umlauf and Burchard, 2003). Near surface deviations between LES and GLS are expected partly due to discretized implementation of the boundary conditions and partly due to parameterization inaccuracy.

Below this surface deviation, $\overline{\epsilon}$ in GLS is similar to $\overline{\epsilon}$ in NOFRONT, in line with the agreement between NOFRONT κ_{eff} and κ from 1D models in section 4. In UNSTABLE, vertically integrated LES $\overline{\epsilon}$ is 26% larger than in NOFRONT (Fig. 5b), reinforcing that submesoscale instabilities enhance dissipation (Thomas and Taylor, 2010; D'Asaro et al., 2014). Less discussed is the suppression of dissipation by lateral advection and its restratification in STABLE (Fig. 5b), with a vertically integrated $\overline{\epsilon}$ that is 20% less than NOFRONT. This compensation between enhanced and suppressed dissipation results in the entire domain having just 1% larger $\overline{\epsilon}$ than the NOFRONT BL turbulence generated by wind input into a homogeneous ocean. The overall dissipation is thus surprisingly similar to that if the submesoscale effects were neglected.

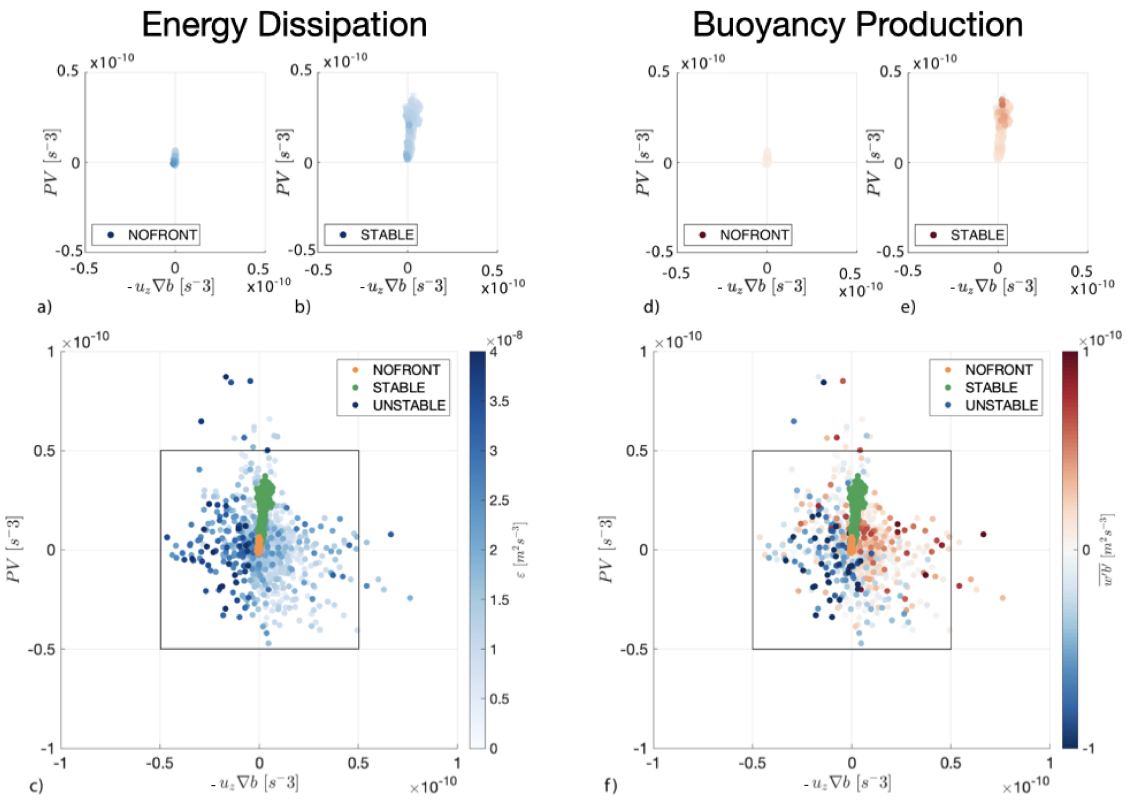

Figure 6. *The correlation between PV (Eq. (12)) and the horizontal advection (ADV) of buoyancy by the horizontal shear, $-d\tilde{u}_i/dz d\tilde{b}/dx_i$ (i.e. a horizontal advective term in the stratification tendency equation). The lower-left quadrant is destratifying flow with negative PV, and the upper right hand quadrant is stratifying flow with positive PV. Dots are colored by magnitude of $\widetilde{w'b'}$ and $\widetilde{\epsilon}$: a) NOFRONT $\widetilde{\epsilon}$, b) STABLE $\widetilde{\epsilon}$, c) NOFRONT, STABLE, and UNSTABLE $\widetilde{\epsilon}$; d) NOFRONT $\widetilde{w'b'}$, e) STABLE $\widetilde{w'b'}$, f) NOFRONT, STABLE, and UNSTABLE $\widetilde{w'b'}$.*

7. Discussion

To further understand the impact of different flow regimes, values of $\widetilde{w'b'}$ and $\widetilde{\epsilon}$ are plotted against the submesoscale PV, $\tilde{q}$ from Eq. 13, and the submesoscale advection (ADV) of buoyancy by horizontal shear, $-\partial\widetilde{u}_i/\partial z\ \partial\widetilde{b}/\partial x_i$ (Fig.6). In regions of negative PV, flow may be subject to instability, including gravitational and symmetric instabilities. Differential advection of buoyancy gradients impacts stratification, with positive ADV increasing stratification and negative ADV reducing stratification. The flow in NOFRONT occupies a narrow region of this parameter space, with homogeneous values of ϵ and $\widetilde{w'b'}$. It was shown that the mixing of buoyancy (section 4) and dissipation of energy (section 6) in NOFRONT agree with estimates from classic BL turbulence theory and are represented by turbulence parameterizations. The rest of this section will focus on STABLE and UNSTABLE, and how these regions differ from NOFRONT and classic BL turbulence theory.

7.1. Stable Region

In STABLE, ADV tends to restratify and tends toward positive PV within this region, with a narrow range of $\widetilde{\epsilon}$ and positive $\widetilde{w'b'}$. The strongest $\widetilde{w'b'}$ occurs in positive PV flows where strong stratification from lateral advection is mixed by wind driven turbulence. Strong PV and enhanced $\widetilde{w'b'}$ are coincident

with attenuated $\widetilde{\epsilon}$ as dissipation of kinetic energy is suppressed in regions of lateral advection and its restratification. Both FRIC and DIA tend to reduce the positive PV in this region (as predicted but overestimated by parameterizations, Fig. 4).

7.2. Unstable Region

The flow in UNSTABLE exhibits larger fluctuations across phase space and in value and sign compared to the other regions, highlighting the heterogeneity of unstable flows and the wide range of processes that contribute to the along front and domain average under downfront winds. Positive ADV tendency co-occurs with the strongest upward flux of buoyancy and smaller values of ϵ: intensive, intermittent restratification with weak turbulence dissipation. Negative ADV tendency, and particularly, though not exclusively, negative PV, are associated with the strongest downward/destratifying flux of buoyancy and the largest rates of energy dissipation: intermittent convective mixing, entrainment, and overturning within the submesoscale features. Overall restratifying, positive ADV wins out in the resolved fluxes which is the opposite of what parameterizations predict (Fig. 4).

A positive buoyancy flux in the presence of mean background stratification implies small scale motions act to mix cold water down (i.e., convection) or include 3D circulations that increase stratification in the presence of stratification. The resulting negative effective kappa (Fig. 3) indicates the fine-scale flow is not isotropic turbulence which would flux down the gradient. Similarly, baroclinic instabilities wrap up to increase local and overall stratification. In the same regions, Symmetric Instability (SI) develops slantwise convection that extracts PV from the thermocline and increases mixed layer stratification and PV. Although the along-isopycnal structures commonly associated with SI (e.g., Haney et al., 2015) are not discernable in this complex flow, the PV and buoyancy fluxes resemble this phenomenon. However, regions of the strongest stratification have lower energy dissipation rates, which is not consistent with the present understanding of ongoing SI (Taylor and Ferrari, 2009).

Conditions for SI arise as down front winds drive down PV at ocean fronts, such that $qf < 0$. Though SI is known to enhance dissipation rates Taylor and Ferrari (2010); Thomas and Taylor (2010), it is intermittent and highly localized. The instability can be active when the ratio between the convective depth (due to unstable Ekman transport), $\widetilde{h}$, and the ML depth, $\widetilde{H}$ is small, or when $h/H << 1$. This ratio is found to obey (Taylor and Ferrari, 2010):

$$\left(\frac{\widetilde{h}}{\widetilde{H}}\right)^4 - c^3\left(1-\frac{\widetilde{h}}{\widetilde{H}}\right)^3\left[\frac{u_*^3}{|\Delta\widetilde{u}_g|^2}cos\theta\right]^2. \tag{19}$$

The SI parameterization put forth by Bachman et al. (2017) requires a threshold of $h/H < 0.9$ for SI to be considered important, with stronger SI occurring as $h/H \to 0$. In the UNSTABLE region, $\widetilde{h}/\widetilde{H}$<0.9 occupies 26% of the domain, whereas $\widetilde{h}/\widetilde{H}$<0.6 occupies 1% of the UNSTABLE domain. Isolating regions $\widetilde{h}/\widetilde{H}$<0.9 does not significantly change ϵ compared to NOFRONT, but the 1% of the region with $\widetilde{h}/\widetilde{H}$<0.6 has 86% higher dissipation than NOFRONT. Overall, there is no correlation between ϵ and ADV or PV.

8. Conclusions and Recommendations

While Monin and Obukhov (1954) and 1D parameterizations do a reasonable job of approximating the turbulent mixing in terms of diffusion, energy dissipated, and potential vorticity sources in between fronts, there are major discrepancies with these theories in both an upfront-wind/Ekman-stabilized front and in a downfront-wind/Ekman-destabilized front, even when separately accounting for the effects of submesoscale mixed layer eddy restratification. A main message from this work is that surface forced boundary layer turbulence is modified–sometimes even reversed in net effect–by the presence of submesoscale flows.

In the UNSTABLE region, a positive mean buoyancy flux in the presence of a stable negative κ_{eff} suggests finescale circulation transports dense fluids as to increase the density gradient. From a broad perspective, this mixing resembles the non-local, upgradient mixing embedded in KPP used to simulate convection during unstable conditions. In KPP, the non-local term is meant to capture the transport of cold water from the surface to depth while ignoring smaller gradients along the way, here, the negative κ_{eff} represents finescale overturning due to a combination of surface cooling, convection from Ekman transport, and submesoscale overturning circulations. While transport equivalent to a net overturning on the submesoscale is expected at submesoscales Fox-Kemper et al., 2008, this diagnosis finds non-negligible finescale up-gradient transport that competes with and often overtakes BL mixing. An examination of PV generated by turbulence in this UNSTABLE region suggests that present parameterizations fail in sign (destruction rather than creation) and magnitude (too large of an effect). This region has the most variations in buoyancy and energy dissipation–indicating a heterogenous collection of restratifying flow in high-PV, counter-gradient, weakly energetic finescale subregions and destratifing flow in low-PV, mixing, strongly energetic plumes. Overall, restratification and positive PV injection dominate in this region in this simulation, which is opposite to what parameterizations predict.

In the STABLE region, turbulence is suppressed, more so than the Monin and Obukhov (1954) expectations due to the increased stratification from lateral advection and the accompanying shallower boundary layer. Consistently, in this region, the potential vorticity tendency and dissipation rates predicted by 1D scalings are overestimated compared to those diagnosed in the simulation.

The Reynolds averaged approach for estimating PV fluxes adopted here lends itself to be compared with what is assumed in numerical schemes for simulations with grid scales too large to resolve finescale motions and instead use BL parameterizations. This can be seen by Leibniz's theorem (see Appendix A) the Reynolds averaged approach results in a loss of information compared to the filtered approach presented by Bodner and Fox-Kemper (2020). The propagation of uncertainty from Leibniz's theorem suggests errors in the frictional and diabatic PV flux terms are orders of magnitude larger than the fluxes themselves. This questions our ability to understand the role of parameterized downgradient turbulent fluxes on PV tendencies in the presence of submesoscale flows.

Submesoscale flows alter the kinetic energy dissipation rate, with ϵ suppressed in regions of lateral restratification–by large scale fronts or intermittent submesoscales–and enhanced in the presence of negative PV and destratifying circulations. While much work has been done to evaluate the enhanced dissipation and mixing due to submesoscales, in this simulation, enhanced dissipation at the downwind front is balanced by turbulence suppression at the upwind front such that the average dissipation is indistinguishable on average over the whole domain from that predicted by BL scalings.

Finally, this simulation is in a modest part of parameter space for the most energetic instabilities, with $M^2 \sim 10^{-8}\,\text{s}^{-2}$, which is more than an order of magnitude less than observed during frontal process studies (e.g. $M^2 \sim\sim 10^{-6}\,\text{s}^{-2}$; Johnson et al., 2020; D'Asaro et al., 2014). Other recent simulations (e.g., Sullivan and McWilliams, 2019) have much stronger fronts but in domains that are too small to resolve mixed layer eddies and the intricate processes as the front destabilizes. More work is needed to extend these results to more energetic frontal cases with varying surface fluxes.

Acknowledgements. We gratefully acknowledge the XXX.

Funding Statement. LJ and BFK were supported by ONR N00014-17-1-2393.

Declaration of Interests. The authors declare no conflict of interest.

Author Contributions. L.J and B.F.K. developed the theoretical framework. L.J led the analysis. L.J and B.F.K wrote the manuscript.

Data Availability Statement. The large eddy simulation snapshots are available at GRIIDC; https://doi.org/10.7266/N7D50KBC.

Ethical Standards. The research meets all ethical guidelines, including adherence to the legal requirements of the study country.

Supplementary Material. Supplementary information are available at (cite H14 and data repository)

References

Aluie, H., Hecht, M., and Vallis, G. K. (2018). Mapping the energy cascade in the north atlantic ocean: The coarse-graining approach. *Journal of Physical Oceanography*, 48(2):225–244.

Bachman, S., Fox-Kemper, B., and Bryan, F. O. (2015). A tracer-based inversion method for diagnosing eddy-induced diffusivity and advection. *Ocean Modelling*, 86:1–14.

Bachman, S. D., Fox-Kemper, B., and Bryan, F. O. (2020). A diagnosis of anisotropic eddy diffusion from a high-resolution global ocean model. *Journal of Advances in Modeling Earth Systems*, 12(2):e2019MS001904.

Bachman, S. D., Fox-Kemper, B., Taylor, J. R., and Thomas, L. N. (2017). Parameterization of frontal symmetric instabilities. i: Theory for resolved fronts. *Ocean Modelling*, 109:72–95.

Belcher, S. E., Grant, A. L. M., Hanley, K. E., Fox-Kemper, B., Van Roekel, L., Sullivan, P. P., Large, W. G., Brown, A., Hines, A., Calvert, D., Rutgersson, A., Pettersson, H., Bidlot, J.-R., Janssen, P. A. E. M., and Polton, J. A. (2012). A global perspective on langmuir turbulence in the ocean surface boundary layer. *Geophysical Research Letters*, 39(18).

Boccaletti, G., Ferrari, R., and Fox-Kemper, B. (2007). Mixed layer instabilities and restratification. *Journal of Physical Oceanography*, 37(9):2228–2250.

Bodner, A. S. and Fox-Kemper, B. (2020). A breakdown in potential vorticity estimation delineates the submesoscale-to-turbulence boundary in large eddy simulations. *Journal of Advances in Modeling Earth Systems*, 12(10):e2020MS002049.

Bodner, A. S., Fox-Kemper, B., Johnson, L., Van Roekel, L. P., McWilliams, J. C., Sullivan, P. P., Hall, P. S., and Dong, J. (2023). Modifying the mixed layer eddy parameterization to include frontogenesis arrest by boundary layer turbulence. *Journal of Physical Oceanography*, 53(1):323–339.

Burchard, H., Bolding, K., and Villarreal, M. R. (1999). *GOTM, a general ocean turbulence model: theory, implementation and test cases*. Space Applications Institute.

Callies, J. and Ferrari, R. (2018). Baroclinic instability in the presence of convection. *Journal of Physical Oceanography*, 48(1):45–60.

Cao, H., Fox-Kemper, B., and Jing, Z. (2021). Submesoscale eddies in the upper ocean of the kuroshio extension from high-resolution simulation: Energy budget. *Journal of Physical Oceanography*, 51(7):2181–2201.

Capet, X., McWilliams, J. C., Molemaker, M. J., and Shchepetkin, A. F. (2008). Mesoscale to submesoscale transition in the california current system. part iii: Energy balance and flux. *Journal of Physical Oceanography*, 38(10):2256–2269.

D'Asaro, E. A., Thomson, J., Shcherbina, A. Y., Harcourt, R. R., Cronin, M. F., Hemer, M. A., and Fox-Kemper, B. (2014). Quantifying upper ocean turbulence driven by surface waves. *Geophysical Research Letters*, 41(1):102–107.

Dauhajre, D. P. and McWilliams, J. C. (2018). Diurnal evolution of submesoscale front and filament circulations. *Journal of Physical Oceanography*, 48(10):2343–2361.

Dong, J., Fox-Kemper, B., Zhang, H., and Dong, C. (2020). The scale of submesoscale baroclinic instability globally. *Journal of Physical Oceanography*, 50(9):2649–2667.

Dong, J., Fox-Kemper, B., Zhang, H., and Dong, C. (2021). The scale and activity of symmetric instability estimated from a global submesoscale-permitting ocean model. *Journal of Physical Oceanography*, 51(5):1655–1670.

Ferrari, R. and Polzin, K. L. (2005). Finescale structure of the t–s relation in the eastern north atlantic. *Journal of Physical Oceanography*, 35(8):1437–1454.

Fox-Kemper, B., Danabasoglu, G., Ferrari, R., Griffies, S., Hallberg, R., Holland, M., Maltrud, M., Peacock, S., and Samuels, B. (2011). Parameterization of mixed layer eddies. iii: Implementation and impact in global ocean climate simulations. *Ocean Modelling*, 39(1-2):61–78.

Fox-Kemper, B. and Ferrari, R. (2008). Parameterization of mixed layer eddies. Part II: Prognosis and impact. *Journal of Physical Oceanography*, 38(6):1166–1179.

Fox-Kemper, B., Ferrari, R., and Hallberg, R. (2008). Parameterization of mixed layer eddies. part i: Theory and diagnosis. *Journal of Physical Oceanography*, 38(6):1145–1165.

Fox-Kemper, B., Johnson, L., and Qiao, F. (2021). *Ocean Mixing*, chapter Ocean Near-Surface Layers. Elsevier. In press.

Fox-Kemper, B. and Menemenlis, D. (2008). Can large eddy simulation techniques improve mesoscale-rich ocean models? In Hecht, M. and Hasumi, H., editors, *Ocean Modeling in an Eddying Regime*, volume 177, pages 319–338. AGU Geophysical Monograph Series.

Garabato, A. C. N., Polzin, K. L., Ferrari, R., Zika, J. D., and Forryan, A. (2016). A microscale view of mixing and overturning across the antarctic circumpolar current. *Journal of Physical Oceanography*, 46(1):233–254.

Gent, P. R. and Mcwilliams, J. C. (1990). Isopycnal mixing in ocean circulation models. *Journal of Physical Oceanography*, 20(1):150–155.

Gula, J., Molemaker, M. J., and McWilliams, J. C. (2014). Submesoscale cold filaments in the gulf stream. *Journal of Physical Oceanography*, 44(10):2617–2643.

Hamlington, P. E., Van Roekel, L. P., Fox-Kemper, B., Julien, K., and Chini, G. P. (2014). Langmuir–submesoscale interactions: Descriptive analysis of multiscale frontal spindown simulations. *Journal of Physical Oceanography*, 44(9):2249–2272.

Haney, S., Bachman, S., Cooper, B., Kupper, S., McCaffrey, K., Van Roekel, L., Stevenson, S., Fox-Kemper, B., and Ferrari, R. (2012). Hurricane wake restratification rates of 1, 2 and 3-dimensional processes. *Journal of Marine Research*, 70(6):824–850.

Haney, S., Fox-Kemper, B., Julien, K., and Webb, A. (2015). Symmetric and geostrophic instabilities in the wave-forced ocean mixed layer. *Journal of Physical Oceanography*, 45:3033–3056.

Held, I. M. and Schneider, T. (1999). The surface branch of the zonally averaged mass transport circulation in the troposphere. *Journal of the atmospheric sciences*, 56(11):1688–1697.

Hoskins, B. (1974). The role of potential vorticity in symmetric stability and instability. *Quarterly Journal of the Royal Meteorological Society*, 100(425):480–482.

Johnson, L., Lee, C. M., D'Asaro, E. A., Wenegrat, J. O., and Thomas, L. N. (2020). Restratification at a california current upwelling front. part ii: Dynamics. *Journal of Physical Oceanography*, 50(5):1473–1487.

Large, W. G., McWilliams, J. C., and Doney, S. C. (1994). Oceanic vertical mixing: A review and a model with a nonlocal boundary layer parameterization. *Reviews of Geophysics*, 32(4):363.

Mahadevan, A., Tandon, A., and Ferrari, R. (2010). Rapid changes in mixed layer stratification driven by submesoscale instabilities and winds. *Journal of Geophysical Research: Oceans*, 115(C3).

Marshall, J. and Radko, T. (2003). Residual-mean solutions for the antarctic circumpolar current and its associated overturning circulation. *Journal of Physical Oceanography*, 33(11):2341–2354.

McWilliams, J. C. (2016). Submesoscale currents in the ocean. *Proceedings of the Royal Society A: Mathematical, Physical and Engineering Sciences*, 472(2189):20160117.

Monin, A. and Obukhov, A. (1954). Basic laws of turbulent mixing in the surface layer of the atmosphere. *Contrib. Geophys. Inst. Acad. Sci. USSR*, 151(163):e187.

Reichl, B. G. and Hallberg, R. (2018). A simplified energetics based planetary boundary layer (epbl) approach for ocean climate simulations. *Ocean Modelling*, 132:112–129.

Skyllingstad, E. D., Duncombe, J., and Samelson, R. M. (2017). Baroclinic frontal instabilities and turbulent mixing in the surface boundary layer. part ii: Forced simulations. *Journal of Physical Oceanography*, 47(10):2429–2454.

Skyllingstad, E. D. and Samelson, R. (2012). Baroclinic frontal instabilities and turbulent mixing in the surface boundary layer. part i: Unforced simulations. *Journal of Physical Oceanography*, 42(10):1701–1716.

Smith, K. M., Hamlington, P. E., and Fox-Kemper, B. (2016). Effects of submesoscale turbulence on ocean tracers. *Journal of Geophysical Research–Oceans*, 121(1):908–933.

Smith, K. S. and Ferrari, R. (2009). The production and dissipation of compensated thermohaline variance by mesoscale stirring. *Journal of Physical Oceanography*, 39(10):2477–2501.

Storer, B. A., Buzzicotti, M., Khatri, H., Griffies, S. M., and Aluie, H. (2022). Global energy spectrum of the general oceanic circulation. *Nature communications*, 13(1):5314.

Su, Z., Wang, J., Klein, P., Thompson, A. F., and Menemenlis, D. (2018). Ocean submesoscales as a key component of the global heat budget. *Nature communications*, 9(1):775.

Sullivan, P. P. and McWilliams, J. C. (2019). Langmuir turbulence and filament frontogenesis in the oceanic surface boundary layer. *Journal of Fluid Mechanics*, 879:512–553.

Sullivan, P. P., McWilliams, J. C., and Moeng, C.-H. (1994). A subgrid-scale model for large-eddy simulation of planetary boundary-layer flows. *Boundary-Layer Meteorology*, 71:247–276.

Suzuki, N. and Fox-Kemper, B. (2016). Understanding Stokes forces in the wave-averaged equations. *Journal of Geophysical Research–Oceans*, 121:1–18.

Taylor, J. R. and Ferrari, R. (2009). On the equilibration of a symmetrically unstable front via a secondary shear instability. *Journal of Fluid Mechanics*, 622:103–113.

Taylor, J. R. and Ferrari, R. (2010). Buoyancy and wind-driven convection at mixed layer density fronts. *Journal of Physical Oceanography*, 40(6):1222–1242.

Taylor, J. R. and Ferrari, R. (2011). Ocean fronts trigger high latitude phytoplankton blooms. *Geophysical Research Letters*, 38(23).

Tennekes, H. and Lumley, J. L. (2018). *A first course in turbulence*. MIT press.

Thomas, L. N. and Lee, C. M. (2005). Intensification of ocean fronts by down-front winds. *Journal of Physical Oceanography*, 35(6):1086–1102.

Thomas, L. N. and Taylor, J. R. (2010). Reduction of the usable wind-work on the general circulation by forced symmetric instability. *Geophysical Research Letters*, 37(18).

Thomas, L. N., Taylor, J. R., Ferrari, R., and Joyce, T. M. (2013). Symmetric instability in the gulf stream. *Deep Sea Research Part II: Topical Studies in Oceanography*, 91:96–110.

Troen, I. and Mahrt, L. (1986). A simple model of the atmospheric boundary layer; sensitivity to surface evaporation. *Boundary-Layer Meteorology*, 37(1-2):129–148.

Umlauf, L. and Burchard, H. (2003). A generic length-scale equation for geophysical turbulence models. *Journal of Marine Research*, 61(2):235–265.

Van Roekel, L., Adcroft, A. J., Danabasoglu, G., Griffies, S. M., Kauffman, B., Large, W., Levy, M., Reichl, B. G., Ringler, T., and Schmidt, M. (2018). The kpp boundary layer scheme for the ocean: Revisiting its formulation and benchmarking one-dimensional simulations relative to les. *Journal of Advances in Modeling Earth Systems*, 10(11):2647–2685.

Verma, V., Pham, H. T., and Sarkar, S. (2019). The submesoscale, the finescale and their interaction at a mixed layer front. *Ocean Modelling*, 140:101400.

Verma, V., Pham, H. T., and Sarkar, S. (2022). Interaction between upper-ocean submesoscale currents and convective turbulence. *Journal of Physical Oceanography*, 52(3):437–458.

Wenegrat, J. O. and McPhaden, M. J. (2016). Wind, waves, and fronts: Frictional effects in a generalized ekman model. *Journal of Physical Oceanography*, 46(2):371–394.

Wenegrat, J. O., Thomas, L. N., Sundermeyer, M. A., Taylor, J. R., D'Asaro, E. A., Klymak, J. M., Shearman, R. K., and Lee, C. M. (2020). Enhanced mixing across the gyre boundary at the gulf stream front. *Proceedings of the National Academy of Sciences*, 117(30):17607–17614.

Whitt, D. B., Lévy, M., and Taylor, J. R. (2019). Submesoscales enhance storm-driven vertical mixing of nutrients: insights from a biogeochemical large eddy simulation. *Journal of Geophysical Research: Oceans*, 124(11):8140–8165.

Wyngaard, J. (2010). Turbulence in the atmosphere.

A. Appendix : Reynolds Average Error Analysis

The along-front and submesoscale mean are both linear operators, which requires the following properties and distinguishes them from more generic "linear filters" more commonly used in LES.

$$\text{idempotence} : \tilde{\tilde{c}} = \tilde{c} = \widetilde{\tilde{c} + c'} = \tilde{c} + \tilde{c'} \rightarrow \tilde{c'} = 0, \tag{A 1}$$

$$\text{idempotence} : \overline{\overline{c}} = \overline{c}, \tag{A 2}$$

$$\text{commutation} : \overline{\tilde{c}} = \tilde{\overline{c}} \equiv c^a = \overline{c^a + c^s} = \overline{c^a} + \overline{c^s} = c^a + \overline{c^s} \rightarrow \overline{c^s} = 0. \tag{A 3}$$

Differentiation and integration are also linear operators, but they do not commute necessarily with averaging. Here we have chosen specific Reynolds averages such that they do, which means

$$\overline{\frac{\partial c}{\partial t}} = \frac{\partial \overline{c}}{\partial t}, \qquad \widetilde{\frac{\partial c}{\partial t}} = \frac{\partial \tilde{c}}{\partial t}, \tag{A 4}$$

$$\tag{A 5}$$

Equation (A 4) is easily implemented, as the averaging does not depend on time. Yet spatial differentiation and integration require a careful interpretation of the periodic boundary condition for the along-front average, and a careful discretization of the submesoscale derivative over the boxcar filter. So while,

$$\overline{\frac{\partial c}{\partial x_j}} = \frac{\partial \overline{c}}{\partial x_j}. \tag{A 6}$$

holds for the along front average, but not for the submesoscale average

$$\widetilde{\frac{\partial c}{\partial x_j}} \neq \frac{\partial \tilde{c}}{\partial x_j}. \tag{A 7}$$

This can be seen by Leibniz's theorem:

$$\frac{\partial}{\partial x_i} \int_{x_1}^{x_2} f dx_j = \int_{x_1}^{x_2} \frac{\partial f}{\partial x_i} dx_j + f(x_2) \frac{\partial x_2}{\partial x_i} - f(x_1) \frac{\partial x_1}{\partial x_i} \tag{A 8}$$

indicating the importance of boundary contributions. Therefore, $\widetilde{\frac{\partial c}{\partial x_j}}$ is simply the difference of end points over the length of the averaging interval, $(c'_{x_2} - c'_{x_1})/L$. Alternatively, $\frac{\partial \tilde{c}}{\partial x_j}$ is centered on the coarse-grained (i.e. submesoscale) grid. This is not relevant for vertical differentiation as there is no averaging in the vertical, which is focus of this analysis. Yet this becomes significant for horizontal differentiation, with an error equivalent to the standard deviation of the endpoint contributions divided by the distance of the end points, or $(\widetilde{c'c'})^{1/2}/(x_2 - x_1)$.

This error is modest when considering the horizontal derivatives of a single variable across a domain. For example, an error estimate for M^2 across the entire unstable region is about 3-7%, which is not significant enough to alter the interpretation of the results. Yet the error estimates increase for submesoscale gradient correlations (Fig. 7), such as those needed for the subPV calculations. In this case the propagated errors become orders of magnitude larger $O(10^{-5} ms^{-2})$ than the submesoscale gradient correlations (e.g. PV $O(10^{-10} ms^{-2})$).

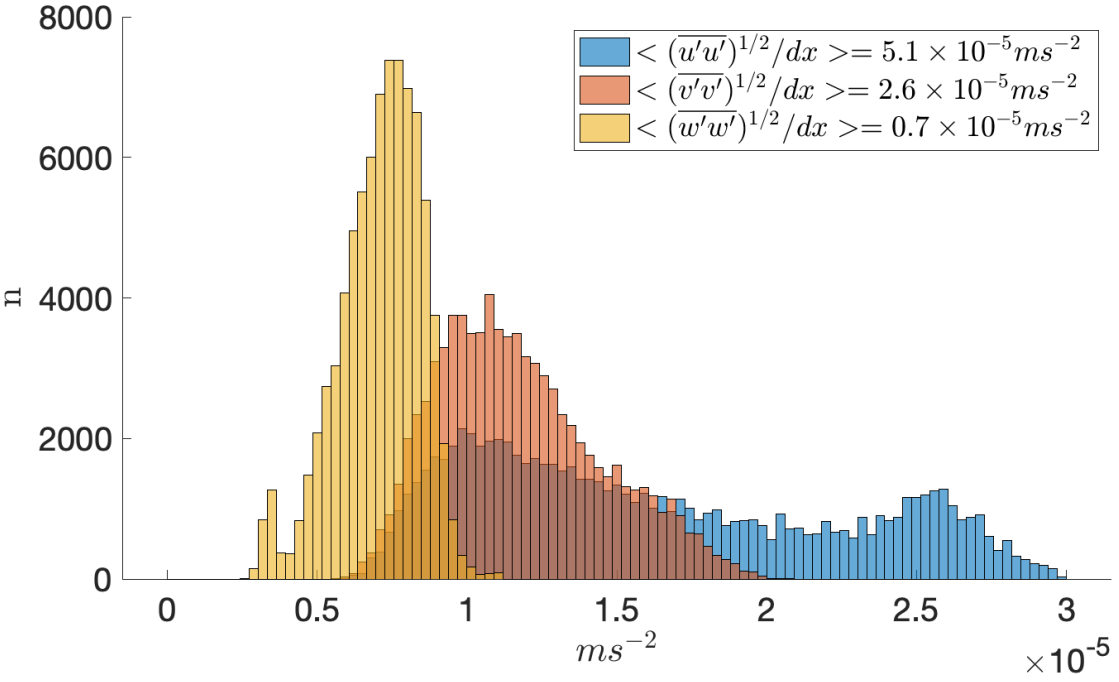

Figure 7. *Histogram of the turbulent flux error in a submesoscale grid. Blue is $\widetilde{u'u'}$, orange is $\widetilde{v'v'}$ and yellow is $\widetilde{w'w'}$.*

B. Appendix B: The Mean Eddy Potential Vorticity Equation

The Reynolds averaged Mean-Eddy PV (MEPV) contains only the mean and submesoscale contributions: $\tilde{\omega}_i = \omega_i^a + \omega_i^s$ and $\tilde{b} = b^a + b^s$, such that Eq. (12) becomes

$$\text{MEPV} = \overline{\tilde{q}} = q^a + \overline{q^s} = \left(f\delta_{k3} + \omega_i^a\right)\frac{\partial b^a}{\partial x_i^a} + \overline{\omega_i^s \frac{\partial b^s}{\partial x_i^s}}, \tag{B 9}$$

where the second term retains the submesoscale gradient correlations in the along front average. Submesoscale PV (the second term on the RHS) is a modest contribution to MEPV, where $\overline{q^s}$ is $1-5\%$ of q^a, yet it will be shown that submesoscale and turbulent fluctuations play a leading order role in MEPV tendencies.

Derivation of the MEPV tendency equation begins with the *submesoscale-permitting* Reynolds averaged buoyancy and momentum equations for $\tilde{c}$ where $c = \tilde{c} + c'$ and $\tilde{c} = c^a + c^s$. Only after forming the PV at this scale is the along-front mean as in section 3 taken. Following Bodner and Fox-Kemper (2020), turbulent transport terms are organized into frictional and diabatic fluxes by defining:

$$\mathcal{F}_i^{a+} = -\frac{\partial}{\partial x_j}\left(\overline{u_i'u_j'}\right) - \mathcal{V}_{ij}^m; \mathcal{F}_i^{s+} = -\left[\frac{\partial}{\partial x_j}\left(\widetilde{u_i'u_j'}\right) - \frac{\partial}{\partial x_j}\left(\overline{u_i'u_j'}\right)\right] \tag{B 10}$$

$$\mathcal{D}^{a+} = -\frac{\partial}{\partial x_j}\left(\overline{b'u_j'}\right) - \mathcal{V}_{ij}^b; \mathcal{D}^{s+} = -\left[\frac{\partial}{\partial x_j}\left(\widetilde{b'u_j'}\right) - \frac{\partial}{\partial x_j}\left(\overline{b'u_j'}\right)\right] \tag{B 11}$$

Eq.(B 10) and Eq.(B 11) differ from Bodner and Fox-Kemper (2020), which adopts a filtering approach to PV not a Reynolds averaged approach. The filtered approach refusing to commute averaging with differentiation retains more accurate information about grid scale gradients that are smoothed by the

Reynolds average. The uncertainty in (B 10) and (B 11) implied by Leibniz theorem (see Appendix A) gives an error estimate for the horizontal derivatives that are an order of magnitude larger than the signal. Yet, this expression is most analogous to what is solved by numerical simulations that use turbulent flux parameterizations. Evaluating PV in this framework, in light of these uncertainties, allows comparison between how PV is modeled in larger grid-scale ocean simulations to the MEPV in the LES.

The buoyancy and momentum equations at the submesoscale (i.e. not averaged yet in the along front direction), become:

$$\frac{\partial}{\partial t}\widetilde{u_i} = \frac{\partial}{\partial t}\left(u_i^a + u_i^s\right) = -\left(u_j^a + u_j^s\right)\frac{\partial}{\partial x_j}\left(u_i^a + u_i^s\right) - \frac{1}{\rho_o}\frac{\partial}{\partial x_i}\left(p^a + p^s\right) - 2\epsilon_{ikj}\Omega_j\left(u_k^a + u_k^s\right) + \mathcal{F}_i^{a+} + \mathcal{F}_i^{s+} \tag{B 12}$$

$$\frac{\partial}{\partial t}\widetilde{b} = \frac{\partial}{\partial t}\left(b^a + b^s\right) = -\left(u_j^a + u_j^s\right)\frac{\partial}{\partial x_j}\left(b^a + b^s\right) + \mathcal{D}^{a+} + \mathcal{D}^{s+} \tag{B 13}$$

The along front average of Eq. (B 12) and Eq. (B 13) recovers Eq. (4) and Eq. (5), respectively. From here, the MEPV tendency equation can be found by multiplying Eq. (B 13) by $\partial/\partial x_i(\partial b^a + \partial b^s)$, and multiplying Eq. (B 12) by $(f\delta_{k3} + \omega_i^a + \omega_i^s)$. Combining the two and rearranging gives:

$$\frac{\partial}{\partial t}\mathrm{MEPV} = -\frac{\partial}{\partial x_i}\Bigg[\underbrace{u_i^a q^a + \overline{u_i^s q^s} + u_i^a\overline{q^s} + \overline{u_i^s\left(\omega^a\frac{\partial b^s}{\partial x_i^s} + \omega^s\frac{\partial b^a}{\partial x_i^a}\right)}}_{\mathrm{ADV}} + \tag{B 14}$$

$$\underbrace{\epsilon_{ikj}\mathcal{F}_j^{+a}\frac{\partial b^a}{\partial x_k} + \overline{\epsilon_{ikj}\mathcal{F}_j^{+s}\frac{\partial b^s}{\partial x_k^s}}}_{\mathrm{FRIC}} - \underbrace{\left(f\delta_{k3} + \omega^a\right)\mathcal{D}^{a+} - \overline{\omega^s\mathcal{D}^{s+}}}_{\mathrm{DIA}}\Bigg] \tag{B 15}$$

Critically to the conclusions of Bodner and Fox-Kemper (2020), note that the finescale c' variables only contribute through their contributions to FRIC and DIA via $\mathcal{F}$ and $\mathcal{D}$, not to MEPV or ADV where only $\tilde{c}$ or c^a and c^s variables contribute. This appendix shows that it is difficult to calculate FRIC and DIA accurately, nonetheless.

Cite this article: Johnson, L. & Fox-Kemper, B. (2023). Modification of Boundary Layer Turbulence by Submesoscale Flows. *Flow*, *1*, E1. doi:XXXX